Seismic analysis of the detachment and impact phases of a rockfall and application for estimating rockfall volume and free-fall height

G. Le Roy, A. Helmstetter, D. Amitrano, F. Guyoton, R. Le Roux-mallouf

Seismic analysis of the detachment and impact phases of a rockfall and application for estimating rockfall volume and free-fall height

G. Le Roy [1, 2], A. Helmstetter [1], D. Amitrano [1], F. Guyoton [2], R. Le Roux-Mallouf [2]

[1]Univ. Grenoble Alpes, Univ. Savoie Mont Blanc, CNRS, IRD, IFSTTAR, ISTerre, 38000 Grenoble, France.

[2]Géolithe, Crolles, France.

Corresponding author: Gaëlle Le Roy (gaelle.le-roy@univ-grenoble-alpes.fr)

Key Points:

- Rockfall detachment, free-fall and impact can be distinguished on a rockfall seismogram
- Seismic energy of the first impact phase is well correlated with the potential energy of the rockfall and allows an estimation of its volume
- Seismic energy and duration of the detachment signal increase with rockfall volume

Abstract

We analyzed 21 rockfalls that occurred in limestone cliffs of the Chartreuse Massif (French Alps). These rockfalls were detected both by Terrestrial Laser Scanning or photogrammetry and by a local seismological network. The combination of these methods allowed us to study relations between rockfall properties (location of detachment and impacts areas, volume, geometry, propagation) and the induced seismic signal. We observed events with different propagation modes (sliding, mass flow, free-fall) that could be determined from Digital Elevation Models. We focused on events that experienced a free-fall after their detachment. We analyzed the first parts of the seismic signals corresponding to the detachment phase and to the first impact. The detachment phase has a smaller amplitude than the impact phase, and its amplitude and duration increase with rockfall volume. By measuring the time delay between the detachment phase and the first impact, we can estimate the free-fall height. We found a relation $Es=aE_p^b$ between the potential energy of a rockfall Ep and the seismic energy E_s generated during the first impact, with parameters $a=10^{-8}$ and $b=1.55$ and with a correlation coefficient $R^2=0.98$. We can thus estimate both the potential energy of a block and its free-fall height from the seismic signals. By combining these results, we obtain an accurate estimate of the rockfall volume. This relation was then tested on different geological settings and for larger volumes using Yosemite and Mount Granier rockfalls. We also compared our results with a data set of controlled releases of single blocks (Hibert et al., 2017) in order to investigate smaller volumes.

1 Introduction

Characterizing rock fall properties such as location, occurrence time, volume and propagation path, is a key point to improve the mitigation of the associated hazards and to better prevent them. Several approaches can be used to detect rockfalls and to assess erosion activity such as satellite imagery or terrestrial and airborne laser scanning. These methods can deliver accurate information on detachment and impact zones and on released volumes and thus provide volume-frequency relationships. However, temporal information is often limited as they rely on the survey lapse times (respectively 2.5, 0.5 and 1 year interval for Dewez et al., 2013; Kuhn & Prüfer, 2014; D'Amato et al., 2016). Hence, with these approaches, it is impossible to resolve the gradual collapse of blocks released from the same location or to determine the relation between rockfalls occurrence and external triggers. This presents significant drawbacks for the knowledge of site activity (number and size of individual events, occurrence time, triggering factor, etc.). In addition, monitoring using DEMs is yet difficult to apply automatically and cannot be used for real-time detection and warning system of rockfalls.

Continuous seismic monitoring provides a solution for this shortcoming as rockfalls can be automatically detected and located from the seismic signal they generate (Battaglia & Aki., 2003, Lacroix & Helmstetter, 2011; Burtin et al., 2013, 2016; Levy et al., 2015, Dietze et al., 2017a). According to the definition given by Varnes (1978), a rockfall is a slope process that involves rock fragment detachment proceeding down the slope by free falling, bouncing, rolling, and sliding until their deposition. All these processes can be identified on the seismic signals. However, as gravitational mass wasting events are complex and composed of several processes occurring simultaneously, it is often difficult to determine the link between block dynamics and the seismic signal generated.

Seismic signals of rockfalls detachment have been identified in several studies (Rousseau et al., 1999; Deparis et al., 2008; Hibert et al., 2011; Dietze et al., 2017b). However, the origin of

these signals was linked to different processes: elastic rebound of the cliff (Rousseau et al., 1999; Deparis et al., 2009; Hibert et al., 2011), fractures opening, and friction between the detached compartment and the cliff (Dietze et al., 2017a). In some cases, the detachment of a rockfall has been preceded by precursory signals. For instance, the 15 000 m^3 Illgraben rock avalanche (Rhone Valley, Switzerland) was preceded by seismic pulses lasting for a few seconds (Zeckra et al., 2015).

Controlled experiments allow an accurate estimation of rockfall properties, and thus a better understanding of the processes generating the seismic signal. Vilajosana et al. (2008) and Bottelin et al. (2014) studied artificially triggered rockfall events. These studies allowed relating the most energetic seismic phases to boulder impacts after a free-fall and showed that impacts were characterized by waves packets with frequency contents over the range 1-50 Hz. Controlled releases of single blocks in a marl gully (Hibert et al., 2017) or in quarries (Saló et al., 2017) explored seismic amplitude and energy in relation to the kinetics of block impacts. Hibert et al. (2017) inferred single block mass and velocity from local seismic records with a fair accuracy (median ratio between calculated and measured velocity of 0.2). In contrast, Saló et al. (2017) did not find a correlation between kinetic parameters of the blocks and measured seismic energies. All these studies highlight the large uncertainties on rockfall properties (volume, velocity, location, etc.) estimated from the associated seismic signal.

In the present study, we analyze Terrestrial Laser Scanning (TLS), photogrammetric and seismic data of natural rockfalls in order to investigate the relations between blocks dynamics and the associated seismic signal. The monitoring of two limestone cliffs, Mount Saint-Eynard and Mount Granier (Chartreuse massif, French Alps), allowed us to obtain numerous data on the characteristics of rockfalls (location, occurrence time, volume, failure mode, etc.).

We select 16 rockfalls from Mount Saint Eynard and Mount Granier that experienced a free fall phase and that were detected both by DEMs and seismic monitoring. We focus on the first part of the seismic signals (detachment and first impact), in order to better understand the link between seismic signals and rockfalls kinetics. This dataset allows us to establish scaling laws between seismic parameters (free-fall duration, frequency, seismic energy) and rockfall characteristics (volume, potential energy, free fall height).

A first data set of Mount Saint-Eynard rockfalls is used as a training data set to determine relations between rockfall properties and the characteristics of the seismic signals. These relations are then applied to a second data set of the Mount Granier rockfalls. Finally, we compare our results with two other sites, in order to test whether our relation could be applied to both smaller and larger rockfall volumes and for different geological settings. In the Yosemite area, we analyze the Happy Isle and Ahwiyah Point rockfalls to investigate volumes larger than 10 000 m^3, while the controlled releases of block of Hibert et al. (2017) extend the range of volumes down to 0.03 m^3.

2 Study sites

2.1. Chartreuse massif

Our main study area is located in the sedimentary cover of the External Crystalline Massifs of the French Western Alps (Figure 1). The Chartreuse massif is mainly composed of limestone and marls forming a succession of synclines and anticlines. The eastern edge of this massif is characterized by long linear limestone cliffs overtopping marly talus slopes. Two major rock formations make up these cliffs: Tithonian stage limestone and Urgonian stage limestone, with near-horizontal beddings. This study area is interesting due to the frequent rockfall activity

covering a large range of volumes, from less than 1 m^3 up to a few thousand cubic meters. Typical failure configurations and triggering factors of rockfalls have been studied in previous studies (Frayssines & Hantz, 2006; D'Amato et al., 2016). These studies inferred that rainfall and freeze-thaw cycles had triggered about half of the rockfall during the studied period (2013-2015).

Mount Saint Eynard is located North East of Grenoble, Isère, French Alps (Figure 1a). It is a long doubled cliff making up the western border of the Isère Valley and the eastern edge of the Chartreuse Massif. It peaks at 1308 m above sea level. Its general morphology consists of two 7 km long subvertical cliffs dipping southeast (Figure 1c). The lower cliff (240 m high) is separated from the 120 m high upper cliff by a forested ledge. The upper cliff consists of massive limestone of the Tithonian stage. The lower cliff consists of fractured thin-bedded limestone, of the Sequanian stage.

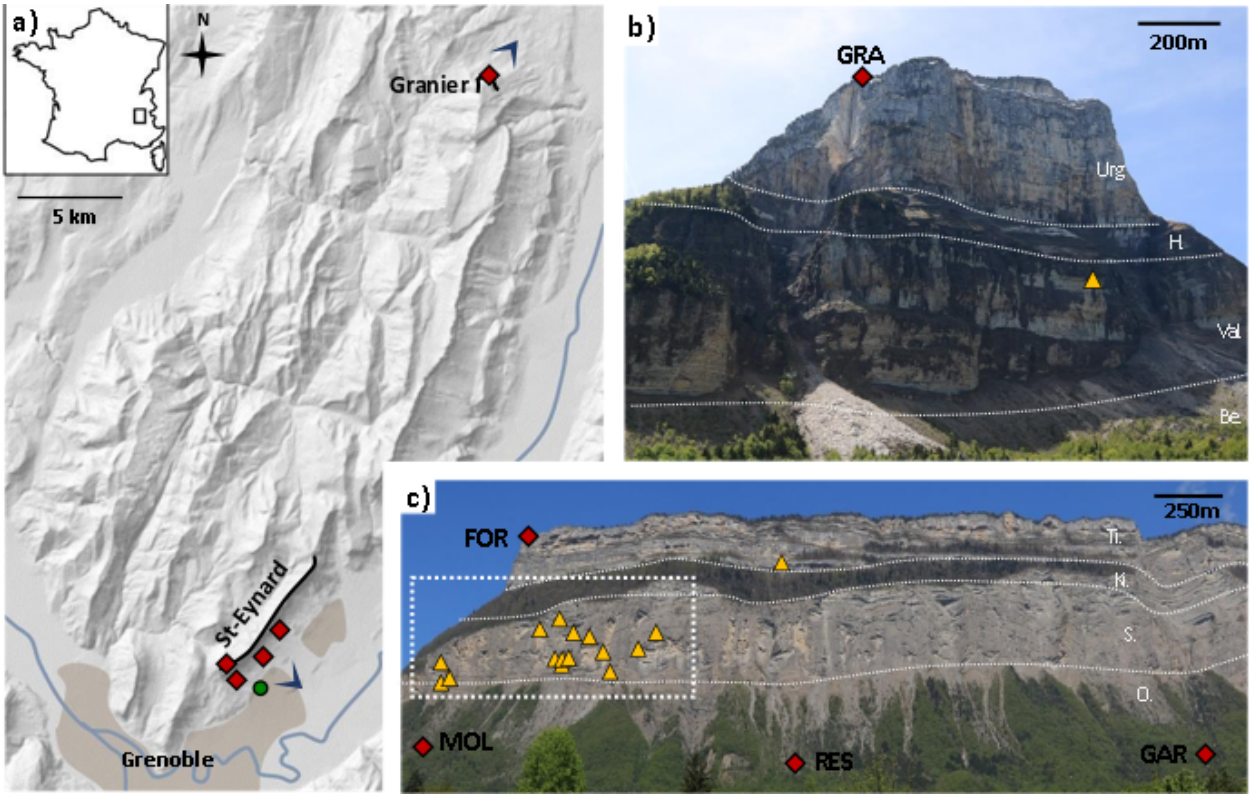

Figure 1. a) DEM of the Chartreuse massif (France), with the location of the photographs shown as blue triangles. b) photograph of the north face of Mount Granier. c): photograph of Mount Saint-Eynard. Red diamonds indicate the location of seismic stations, green dot is the camera enabling a time lapse monitoring of the cliff. Dashed rectangle: area monitored by TLS survey and by a photographic time lapse survey. Yellow triangles: location of origin of rockfall detachment areas. Stage formations: Urg. Urgonian limestone, H. Hauterivian marls, Val. Valanginian limestone, Be.Berriasian marls, Ti. Tithonian limestone, Ki. Kimmeridgian marls, S. Sequanian limestone, O. Oxfordian marls.

Mount Granier (1933 m ASL), located north of the Chartreuse massif (Figure 1b), is an iconic mountain affected, in 1248, by one of the biggest landslides in Europe (500 million m^3,

Nicoud et al., 1999). Its north face, a 800 m high rock wall that appeared after the landslide, forms a natural geological cross section in Urgonian limestone, Hauterivian marls, Valanginian limestone and Berriasian marls. Formed by perched syncline oriented to the east, the Mount Granier presents numerous fractures and karst network.

2.2 Other sites

Yosemite Valley is a deep, glacier-carved valley bounded by steep granite cliffs. These steep cliffs produce numerous rockfalls and rockslides, which range from small boulders to massive events of several million cubic meters. In this study, we focus on three events exceptional due to their size and induced damages: the Happy Isles rockfall, which occurred on July 10, 1996 (Morrissey et al., 1999; Wieczorek et al. 2000) for which two large rockfalls of combined volume estimated between 23 000 and 38 000 m^3 broke loose from cliffs adjacent to the Happy Isles Nature Center. The impact of these blocks generated pressure waves that downed over 1000 trees, destroyed a bridge and caused one fatality and several injuries. Finally, the unusually large rockfall (25 400 m^3, which dislodged en route 21 300 m^3) occurred in 2009 near Ahwiyah Point.

controlled release of single blocks within a soft-rock (black marls) gully of the Rioux Bourdoux torrent (French Alps). 28 blocks, with masses ranging from 76 kg to 472 kg

For more details …. Blablabla …. see Hibert et al. (2017)

2.3 Instrumentation

2.3.1 Mount-Saint-Eynard

Mount Saint-Eynard has been monitored since 2013 by several methods. The south of the Mount Saint-Eynard has been yearly surveyed by TLS since 2009, using an Optech Ilris-LR laser scanner, along a 750 m zone of interest (Guerin et al, 2014; D'Amato et al. 2016). In this study, we focus on rockfalls detected at the Mount Saint-Eynard cliffs between November 2013 and December 2015. In order to monitor a larger area, located between the seismic stations MOL and GAR (Figure 1c), and to reduce the delay between TLS surveys (once a year), we have carried out sporadic photogrammetric surveys over a larger area and to analyze specific events.

The cliffs are also monitored using an autonomously operating camera Canon EOS Rebel T3 1100D (Figure 1c) taking photographs every 10 min.

In 2013, four broad band 3-components seismometers (Guralp CMG40T, with a corner frequency of 0.1 Hz and a sampling frequency of 100 Hz) have been installed a few hundred meters apart, in order to detect rockfall activity. Stations MOL, RES and GAR are located at the cliff foot on top of scree, while station FOR is located on the cliff head, on top of rock (Figure 1c).

2.3.2 Mount Granier

There were no TLS or photographic time lapse surveys at Mount Granier. Therefore, we used sporadic photogrammetry surveys to reconstruct DEMs.

In 2016, a series of rockfalls occurred at Mount Granier with volumes up to 75 000 m^3 (Hobléa et al., 2018). In order to monitor the Mount Granier rockfall activity following these rockfalls, station, GRA, was installed on the cliff head of Mount Granier (Figure 1) in June 2016.The seismometer was a 3-component velocimeter with a corner frequency of 2 Hz. The signal was sampled at 250 Hz. When events were seismologically detected, complementary photogrammetric surveys were carried out within the next week.

2.3.3 Yosemite Park

Yosemite Park rockfall events are occasionally energetic enough to be detected by regional seismic sensors located several tens of kilometers away. Two notable examples are the 1996 Happy Isles rockfalls (Wieczorek et al., 2000; Morrissey et al., 1999) and the 2009 Ahwiyah Point rockfall (Zimmer et al., 2012) which are studied here.

In the case of the Happy Isles rockfalls, although the entire rock-fall event was not observed, rockfall characteristics used in this study were reconstructed by Morrissey et al. (1999) and Wieczorek et al. (2000) from eyewitness accounts, seismic records and field evidence.

Airborne LiDAR data were collected in 2006 and in 2010 following the Ahwiyah Point rockfalls, by the National Center for Airborne Laser Mapping (NCALM). A complementary terrestrial LiDAR was carried out in May 2009, two months after the Ahwiyah Point rock fall, using a Riegl Z420i instrument, from two scan positions located 1150 m from the Ahwiyah Point rockfall source area (Zimmer et al., 2012).

3. Methods

3.1. Topographic data analysis

Repeated topographic surveys allow identifying missing rock mass volumes, which can be interpreted as result of rockfalls and provide information on its detachment area, impact area, volume, free-fall height and failure mechanism. DEMs were constructed both by TLS for Mount-Saint-Eynard (D'Amato et al., 2016) and by photogrammetry (Mount Saint Eynard and Mount Granier, in this study).

Mount Saint-Eynard photogrammetric surveys were carried out using data sets of more than 500 photographs (camera Canon EOS 7D, resolution 5-9 cm/pixel) taken from 12 locations at the base of Mount Saint-Eynard. Three Mount Granier photogrammetric surveys were carried out between January and February 2017, providing a dataset of 100 photographs taken from eight locations (resolution < 8 cm/pixel).

Point clouds were constructed using Structure from motion (SfM) technics with Agisoft Photoscan software. Raw point clouds were cleaned, in order to remove vegetation noise and keep only the rock surface. They were georeferenced using a georeferenced point cloud of the site obtained by airborne laser scanning in 2011. The co-registration (or alignment) of the scans is achieved first by a manual alignment, which consists in identifying common points in the different point clouds. Following this rough matching, we applied an automated iterative procedure with a point-to-surface Iterative Closest Point (ICP) algorithm (Besl and McKay, 1992; Teza et al., 2007), in order to minimize the co-registration errors.

The quality of photogrammetric surveys is slightly coarser than TLS surveys (mean points distance for photogrammetric surveys: 15 cm, TLS surveys: 10 cm).

Once raw point clouds are cleaned from vegetation noise, they are georeferenced using a georeferenced 1 m spacing DEM of the site (from the IGN, French National Institute of Geography) and then meshed. We considered negative deviations larger than a threshold (TLS:10 cm; photogrammetry: 30 cm, corresponding to a 99.5% quantile of the noise distribution of the distance between the two point clouds) as rockfalls. The point clouds defining a fallen compartment are then meshed.

3D reconstructions provide constraints on the morphology of the fallen compartments. For each event, volume, surface and geometry (length, width, depth and gravity center) can be determined. For Mount-Saint Eynard area, this work was primarily carried out by D'Amato et al. (2016). They determined the volume and geometry of the detected events. We reprocessed these TLS point clouds to retrieve complementary information (volume uncertainty, free-fall height, cliff profile).

Based on these characteristics and by considering that the main force involved in the process is gravity, we can determine failure mechanisms. Depending on the weight vector characteristics (built from the gravity center, Figure 2a, 2b), two main types of failure were considered, (i) slide and (ii) free-fall or topple. When the weight vector intersects the cliff, the mechanism is a slide (Figure 2a). When it intersects a free face, the failure type is free-fall (Figure 2b) or topple. Topple involves a forward rotation out of the slope of the compartment about an axis below the center of gravity of the compartment (Cruden & Varnes, 1996). This kind of failure is likely to occur if the lower part of the compartment is intact whereas fractures are present in its upper part. For topple or free-fall detachment, no, or little, shear displacement takes place, contrary to slide failure. Topple and free-fall could not be distinguished in this study due to the lack of information on the repartition of fractures before failure. We thus use the term "free-fall" to designate both free-fall and topple mechanisms in the following.

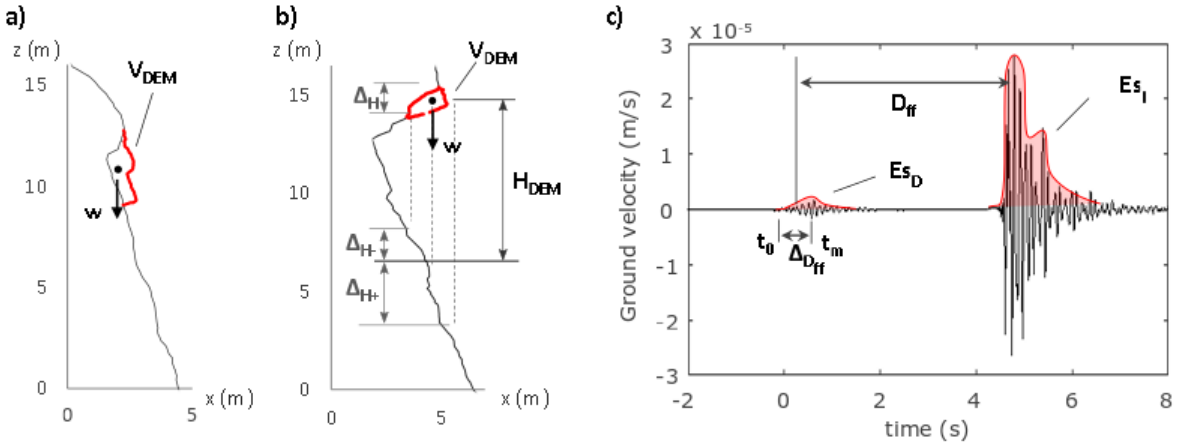

Figure 2. Definition of the metrics used in this study using (a., b.) DEM of the cliff and (c.) rockfalls seismic signals of the 01.18.2015 event. a) cliff profile of the 02.02.2015 event presenting a sliding failure mechanism, b) cliff profile of the 15.08.2014 event presenting a free-falling failure mechanism. The black arrow represents the weight vector w built from the gravity center.

Some rockfalls experienced a free-fall after their detachment. In this case, the free-fall heights are obtained by measuring the distance H_{DEM} between the gravity center of the compartments and their vertical projections on the cliff face. As illustrated in Figure 2b, Δ_H the uncertainty on H_{DEM} depends on the size of the compartment and on the angle of the slope, e.g., a steeper slope induces a larger uncertainty. The 25.11.2015 event underwent a 2 m slide after its detachment. In this case, the impact location and free-fall height were constrained by clear impact marks observed on the field. Using the DEMs, we can also calculate the potential energy of a rockfall Ep_{DEM} before its impact.

$$Ep_{DEM} = p\ V_{DEM}\ g\ H_{DEM}, \quad (1)$$

where V_{DEM} is the volume, p is the density and g=9.82 m.s^{-2} is the gravity constant.

3.2 Detection and classification of seismic signals

A rockfall event is characterized by a series of pulses of ground velocity with frequency contents between 5 and 50 Hz and duration between several seconds and about one minute (Dietze et al., 2017a, Provost et al., 2018). This characteristic pattern makes rockfalls distinct from other sources, such as earthquakes and anthropogenic noise. We have used the method of Helmstetter and Garambois (2010) in order to detect seismic events. The detection is performed by analyzing the seismic energy between 2 and 20 Hz averaged over all stations. An event is detected when the amplitude exceeds the long-term average by a factor of 3 or more. Events that are also detected by the regional seismic network Sismalp are automatically classified as earthquakes. We check all events in order to classify them based on the properties of rockfall seismic signals described in previous studies (Helmstetter and Garambois, 2010; Provost et al., 2018). The configuration of the network, with large distances between stations, does not allow us to use the apparent velocity or the inter-trace correlation as classifying parameters. Earthquakes are characterized by distinct P and S waves, and have similar waveforms on all stations (amplitude, frequency content and shape of envelope). Rockfalls usually display a more complex envelope, with a succession of peaks corresponding to successive block rebounds. Events that are only visible at one station are likely noise (e.g., road traffic). Wind, rainfall and storms also generate seismic signals, which can be recognized by their relatively high-frequency content (mostly above 20 Hz) and by a large variability of signal properties between stations. For signals with ambiguous waveforms, we checked the seismic signal at nearby seismic stations from the regional network Sismalp to help distinguishing earthquakes from rockfalls. The small number of sensors and the large distance between sensors do not allow an accurate source location. Signals are emergent, therefore manual picking is difficult, and uncertainty can be as large as 1 second, leading to large location errors. The large distances (several hundred meters) between sensors make inter-sensor correlation very weak and does not allow the use of beam-forming methods (Lacroix and Helmstetter, 2011; Dietze et al., 2017a). Nonetheless, we can obtain some information about the source location from manual picks of the seismic signals and from amplitude ratios (corrected from site effects). The rockfall is likely located closest to the station with the strongest amplitude. This information is only used to select rockfalls that are likely located within the study area.

3.3 Characterization of rockfalls from seismic signals

In order to compare characteristics of the seismic signals and rockfalls dynamics, we use five metrics extracted from either the seismograms or the DEMs: seismic energy of the detachment phase E_{sD}, seismic energy of the impact phase E_{sI}, free-fall duration D_{ff}, rockfall volume measured V_{DEM} and free-fall height H_{DEM} measured on the DEMs. Figure 2 presents an overview of the different metrics.

To calculate the seismic energy E_s, we assume a point-source (Kanamori & Given, 1982; Eissler & Kanamori, 1987) and we consider the medium as isotropic and homogeneous. We also consider that surface waves dominate the seismic signal (Dammeier et al., 2011; Levy et al., 2015; Levy et al. 2018). Signals were band-pass filtered between 2 and 50 Hz for the entire analysis.

The following relations were used:

$$E_s = 2\pi rphc \int_{t_0}^{t_1} u_{env}(t)^2 e^{\alpha r} \varepsilon \, dt \quad (2)$$

$$u_{env}(t) = \sqrt{u(t)^2 + H(u(t)^2)} \quad (3)$$

$$u(t) = \sqrt{u_E^2(t) + u_N^2(t) + u_Z^2(t)} \quad (4)$$

where t_0 and t_1 are the manually picked onset and end times of the seismic signal, r is the distance between the event and the recording station, h is the thickness of the layer through which surface waves propagate, p is the ground density, c is the phase velocity of the seismic waves, $u_{env}(t)$ is the envelope of the ground velocity $u(t)$ obtained using the Hilbert transform (H), α is a damping factor that accounts for inelastic attenuation of the waves (Aki and Richards, 1980) and ε a coefficient accounting for site effects. Uncertainties on the distance, frequency, ground density, attenuation factor and wave velocity are taken into account in the calculation of seismic energy.

The distance between the detachment zone and the stations is well constrained by DEM data. For free-fall events, the distance between the impact area and each station is determined as the distance between the station and the intersection of the vertical projection of the compartment gravity center and the cliff face. We considered that this distance was prone to a maximal error of 20 m for Mount Saint-Eynard and 30 m for Mount Granier, due to the size of the block and to the slope angle in the impact zone (see Figures 2b and 3c).

We have estimated the seismic wave velocity from the location of rockfalls estimated form the TLS surveys and from the manual picking of the first impact for all stations and all rockfalls detected at Mount Saint Eynard. We search for the velocity V that minimizes the residuals on the differential travel times. For each rockfall and each couple of stations i,j, we estimate the difference in arrival times t_j-t_i. The theoretical travel time delay is $(r_i$-$r_j)/V$. Minimizing the differences between the observed and theoretical time delays allows us to estimate V=1810 ±100 m.s^{-1} (Figure 4a).

We assume a density of 2500 ±100 kg.m^{-3}. The frequency centroid of the impact seismic signals averages at 10 ± 2 Hz. Therefore the thickness was taken as one wavelength of Rayleigh waves, h=181 ± 20 m for a frequency of 10 Hz.

We have estimated the site effect coefficient ε using a catalog of 200 earthquakes recorded by the Mount Saint-Eynard network and located by the regional seismic network Sismalp. We have computed the ratio of amplitude at stations MOL, GAR and RES over the reference station FOR

located at the cliff head. This way we were able to correct the amplification at each station (Borcherdt, R.D, 1970). Site effect of Mount Granier was computed using 4 earthquakes recorded by the reference station FOR and by station GRA.

In order to estimate the attenuation factor, we used the relationship derived by Kanai et al. (1984):

$$\left[\frac{a_i}{a_j}\left(\frac{r_i}{r_j}\right)^n\right] = \left(\frac{\varepsilon_i}{\varepsilon_j}\right) - \alpha(r_j - r_i) \quad (5)$$

with a_i and a_j the maximum amplitudes at two stations filtered around the frequency centroid, between 9 and 11 Hz, n = 0.5 for surface waves, r_i and r_j the corresponding epicentral distances, and ε_i and ε_j constants depending on the ground and installation conditions of each sensor. This method has also been used in previous studies of rockfalls (Levy et al., 2015; Hibert et al., 2017).

Since we have estimated the site effects term ε for each station, we can normalize each signal by this factor and rewrite (5) as

$$\left[\frac{a_i\varepsilon_j}{\varepsilon_i a_j}\left(\frac{r_i}{r_j}\right)^n\right] = -\alpha(r_j - r_i) \quad (6)$$

We can thus estimate α from a linear regression using Equation (6). We have selected seismic records of the rockfalls detected at Mount Saint Eynard (listed in Table 1) at all stations. Using the location derived from the topographic analysis, we have estimated $\alpha = 8.8 \times 10^{-4}$ m^{-1} (Figure 4b) with a regression uncertainty of $\pm$ 0.9 x10^{-4} (confidence interval 68%). This factor is sensitive to the choice of the frequency band. Thus, as the centroid frequency of the impact phase has been determined as 10 ± 2 Hz, the lower bound of α has been set to 6.9 x10^{-4} m^{-1} (frequency 8 Hz) and the upper bound to 10.3 x10^{-4} m^{-1} (frequency 12 Hz).

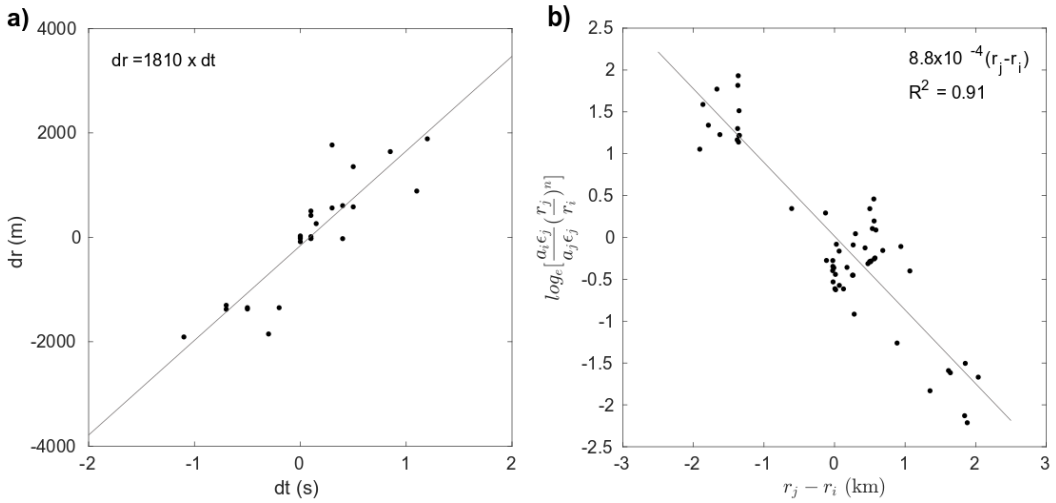

Figure 4. a) Estimation of the seismic wave velocity. For each rockfall detected at Mount Saint Eynard and each couple of stations, we plot the difference in source-station distance *dr* as a function of the time delay between the impact time detected on each seismogram. (b) Estimation of the attenuation factor α using equation (6) with *n*=0.5.

There is only one station at Mount Granier, therefore we cannot estimate seismic wave velocity or the damping factor. We thus assume that material parameters (*V, h, p, c* and α) are the same as for the Mount Saint-Eynard's, since the geological context is similar in both cases.

Seismic energy can also be derived from the Gutenberg-Richter magnitude-energy relation with m the magnitude (Kanamori and Anderson, 1975).

$$\text{Log } E_s = 1.5m + 4.8 \quad (7)$$

This relation was used for the Yosemite rockfalls and for the dataset of controlled block releases (Bibert et al., 2017).

When the fallen compartment undergoes a free-fall immediately after its detachment, the seismic signal of the detachment phase can be isolated from the blocks propagation. In our dataset, when the seismic signal of the detachment and first impact are not overlapping, it is possible to calculate the free-fall height H_s by measuring the free-fall duration D_{ff}:

$$H_s = \frac{{D_{ff}}^2 . g}{2} \quad (8)$$

where g is the gravity constant (9.81 m/s²). The impact time is determined on the seismograms at the maximum amplitude of the impact phase. To determine the detachment time, we chose to calculate it by averaging the initial time of the detachment phase t_0 and the time of maximum amplitude t_m (see Figure 2c).

4. Rockfall databases

We have constructed a database of rockfalls at Mount Saint Eynard and Mount Granier by coupling topographic surveys and seismic monitoring. We tried to associate each rockfall detected using DEMs with a rockfall seismic signal. We also analyze two other datasets, Yosemite rockfalls and controlled releases of blocks, in order to extend the range of rockfall volumes.

4.1 Rockfall catalogs obtained by topographic data

The south of the Mount Saint-Eynard has been yearly surveyed by TLS along a 750 m zone of interest. This survey allowed the detection of events with volumes as small as 0.01 m^3. Overall, D'Amato et al. (2016) have detected 508 events by TLS comparison between November 2013 and April 2015.

There was no regular monitoring of Mount Granier using TLS or photogrammetric surveys. Rockfalls were first detected by the seismic station GRA. After these events, we reconstructed DEMs of the cliff based on existing photographs taken before the rockfalls and we performed photographic surveys after the rockfalls.

4.2 Rockfall catalogs obtained by seismic monitoring

4.2.1 Mount Saint Eynard

At Mount Saint-Eynard, we have detected several thousand events between November 2013 and December 2015, Most of these events have been classified as noise (electronic noise, road traffic, helicopters, storms…). Most of the remaining events (740) are likely seismic signals. Most of these events have also been detected by the regional seismic network Sismalp. We found only 87 events that could be identified as rockfalls. Among these events, 46 events were ruled because the seismic signal had a stronger amplitude at station RES and GAR compared to station MOL, indicating that they were likely located outside of the area monitored by the photographic time lapse survey. This spatial distribution of event (about 50% of events located between stations MOL and RES) is consistent with the data provided by photogrammetric surveys, which cover the area located between stations MOL and GAR (40% of the events detected by photogrammetry occured between stations MOL and RES.). We also discarded all events detected by only one seismic station (7 events).

4.2.2. Mount Granier

At Mount Granier, thousands of events were also detected between June 2016 and June 2017. Most of these events likely originate from the cliff just under station GRA, where a large rockfall occurred on May 2016 (Hobléa et al., 2018). Most events were indeed very short and high frequency. On the night of January 17th-18th 2017, we detected two events with amplitudes and duration much larger than all preceding events. Between these two large events, we also detected two smaller events, with similar waveforms but smaller amplitudes. Another seismic signal with similar properties was detected on February 1st 2017.

4.3. Association of topographic and seismic data

4.3.1 Mount Saint-Eynard rockfalls

In order to associate events detected by TLS to those seismologically detected, we used the dating periods determined using the time-lapse photographic survey. This information allows us to associate events detected by TLS to those seismologically detected. In several cases, especially during winter when nights are longer and weather conditions unfavorable, several events can be distinguished within a pair of photographs. In this case, it is impossible to associate unambiguously events detected by TLS and by the seismic network. In order to avoid any mismatch, if several events had occurred within a pair of photographs, these events were ruled out.

One event detected by photogrammetry at the Mount-Saint-Eynard was added to this catalog (25.11.2015-03:54:39). This event, located outside of the area monitored by the photographic time lapse survey, could not be accurately dated making the association with seismically detected events ambiguous. During the time interval between two photogrammetric surveys (27 days), three rockfalls have been detected by the seismic network. Among these events, two events likely occurred near station MOL, because the amplitude at station MOL was much larger than at station GAR. The last event had similar amplitudes at stations MOL and GAR, in

agreement with the rockfall location determined by photographic survey in between MOL and GAR. This allowed us to associate the event detected by photogrammetry to its seismic signal.

4.3.2 Association of photogrammetric and seismic data of Mount Granier rockfalls

Field observations on January 20, 2017 revealed the occurrence of a recent rockfall on the north face of Mount Granier. It was clearly visible as the rock deposits were not covered by snow. Since the last snow fall occurred on January 14, it provides a strong constraint on the date of occurrence, and allows us to associate this rockfall with the seismic signals recorded at station GRA on January 17th-18th 2017 (events A_1, A_2, A_3, A_4 in Table 1). Another seismic signal with similar properties was detected on February 1st (event B). It can be associated with another rockfall that occurred at the same location and that can be dated from photographs taken the 2nd of February 2017.

By constructing DEMs using photogrammetry, we could locate and measure the volume of the event of February the 1rst. However, due to the quick succession of the first sequence of rockfalls, we were only able to build a 3D model corresponding to the cumulated volume of the $A_{1\text{-}4}$ sequence (Figure 3, Table 1).

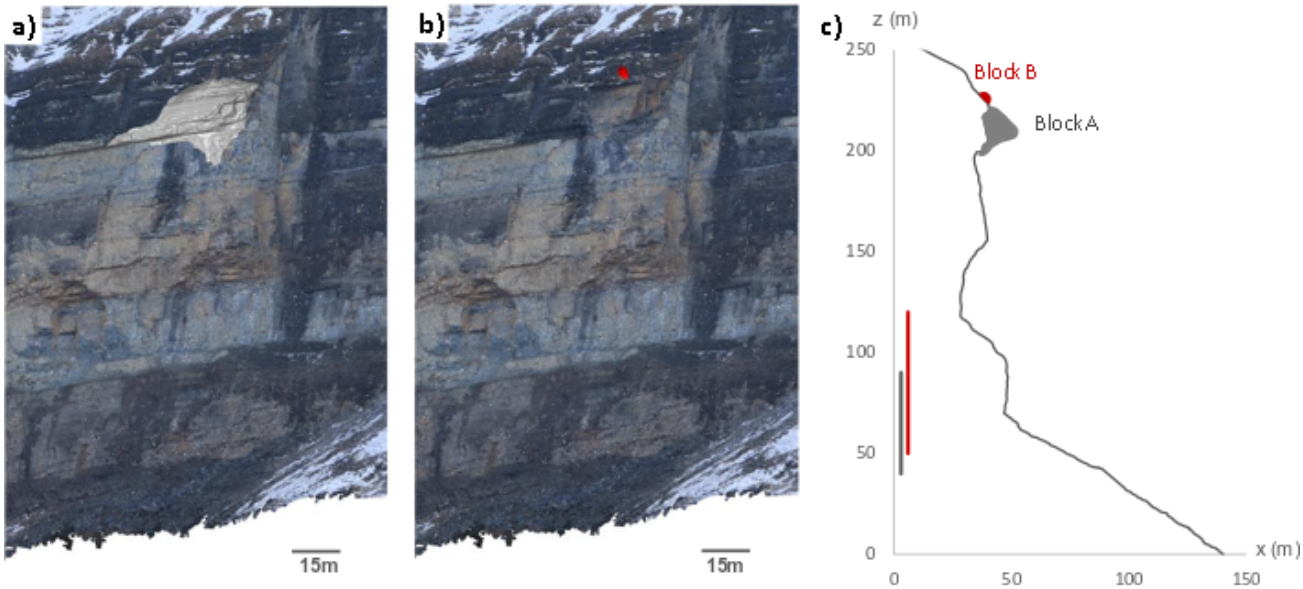

Figure 3. a) Illustration of the set of events $A_{1\text{-}4}$ (January 17th-18th 2017), photographs taken January 19th, in grey: rockfall compartment, b) DEM of the event B (February 1st 2017), photographs taken February the 2nd, in red: rockfall compartment, c) cliff profile with the event location in red. Colored lines: calculated impact areas of events A and B obtained from the DEM.

4.4. Characteristics of selected rockfalls for Mount Saint Eynard and Mount Granier

By coupling DEM and seismologic methods, we have compiled a catalog of 16 rockfalls that occurred at Mount Saint-Eynard between November 2013 and December 2015 with an accurate time, location, geometry and volume (Table 1). The volume of these events ranges from

1.4 m^3 to 1550 m^3. Among these 16 events, it is possible to distinguish the detachment phase for 10 events. This catalog is completed by five rockfalls that occurred at Mount Granier.

Mount Saint Eynard is better instrumented than Mount Granier (regular TLS and time-lapse photographic surveys, more seismometers). Therefore, rockfall parameters (volume, free fall height, seismic energy,...) are better constrained. We thus use this site as a training dataset in order to build scaling laws between rockfalls properties (volume, free-fall height, potential energy) and seismic parameters (seismic energy, free-fall duration). Results are then tested on the other sites. Mount Granier has a similar geological setting than Mount Saint Eynard and allows us to extend the range of investigated volumes and free-fall heights.

4.5 Other datasets: controlled releases of blocks and Yosemite park rockfalls

We analyze three very large rockfalls that occured in Yosemite valley, with well constrained parameters, in order to test how seismic energy scales with rockfall volume. The rockfalls were detected by regional seismic sensors located several tens of kilometers away. The first two events, Happy Isles rockfalls, occurred on July the 10th 1996 (Morrissey et al., 1999; Wieczorek et al. 2000; Stock et al., 2013). Rockfall characteristics were reconstructed by Morrissey et al. (1999) and Wieczorek et al. (2000) from eyewitness accounts, seismic records and field evidences. Four separate events occurred within a short time interval. The first two events, which mobilized between 23000 and 38000 m^3 of granite, experienced a 550 m free fall. The impact at the base of the cliff generated seismic waves with magnitudes of 1.55 for the first block (block A) and 2.12 for the second block B (Morrissey et al., 1999). Seismic energies ($1.33x10^7$ J and $9.5x10^7$ J for respectively block A and B) were inferred from the magnitude using Equation (7). Stock et al. (2013) estimated that the volume of block A represented about 15 to 20% of the total volume. In this study, we thus assume a volume of 3450-7600 m^3 for block A and 15450-34500 m^3 for block B. These two blocks slid down a steeply inclined ramp or shelf and then fell on a ballistic trajectory about 500 m before hitting the northern part of a talus slope at the base of a cliff. In order to estimate the potential energy of these events, we use two extreme free fall heights: 665 m, which represents the total height from the point of origin of the blocks to the base of the cliff, and 500 m, which represents only the height for which the block fell with a ballistic trajectory. This way we estimate that the potential energy of block A was ranging between $4.5x10^{10}$ and $1.3x10^{11}$ J and for block B between 2.0 and $5.9x10^{11}$ J.

The third event occurred in 2009 near the summit of Ahwiyah Point. The rockfall involved a block of volume 27 400 ± 1370 m^3 that slid off a ramp after its detachment and fell approximately 350 m down the northwest face of Ahwiyah Point. It then impacted a prominent ledge, which induced the dislodging of additional material. The combined debris then tumble down the cliff over an additional 300 m. The rockfall volume was estimated from airborne LiDAR surveys collected in 2006 and 2010 (Zimmer et al., 2012). This event was detected on seismic networks as far away as 350 km and was measured as a magnitude 2.4 (seismic energy $2.5x10^8$ J). Zimmer et al. (2012) studied this event and its dynamics and trajectography. They determined that the primary seismic signal was induced by the impact, at a high velocity of the falling block (73±5 m/s), on a prominent ledge 300 m below the bottom of the source area. This way, the kinetic energy of the falling block before impact was estimated to 4.0±0.75 $x10^{11}$ J.

Finally, we compare our results with the controlled releases of single block performed by Hibert et al. (2017).

Controlled release blocks data set : number of events, range of volume and kinetic energy

Site	Event	Dating interval	Failure mechanism	Volume V_{DEM} (m^3)	Volume V_{EsD} (m^3)	Volume V_{EsI} (m^3)	Free-fall height DEM (m)	Free fall height (m)
Saint-Eynard	04.11.2013 19:35:36	1 day	topple	1.4 ± 0.1	1.8 - 3.0	0.5 - 0.9	37 - 67	31 - 44
	16.11.2013 22:11:37	1 day	topple	13.6 ± 0.1	3.2 - 5.9	3.0 - 14.8	6 - 11	12 - 19
	25.11.2013 06:44:54	10 min	topple	3.2 ± 0.1	5.3 - 11.2	1.3 - 6.4	12 - 38	21 - 37
	06.12.2013 04:25:05	2 days	topple	6.1 ± 0.1	2.7 - 5.7	4.5 -19.2	19 - 28	24 - 28
	30.12.2013 23:27:19	1 day	topple	5.1 ± 0.1	2.5 - 4.6	2.2 - 9.0	12 - 38	36 - 48
	07.02.2014 22:00:40	2 days	topple	1.9 ± 0.1	-	-	0 - 1	-
	08.02.2014 19:48:44	10 min	sliding	1546.5 ± 5	-	-	0	-
	15.08.2014 01:08:33	1 day	topple	5.3 ± 0.2	2.7 - 4.5	2.4 - 10.1	6 - 17	16 - 24
	07.01.2015 08:45:12	1 day	topple	1.2 ± 0.1		-	0 - 1	
	18.01.2015 08:20:13	1 day	topple	100.4 ± 0.2	51.0 - 160.1	40.4 -182.4	79 - 82	65 - 88
	22.01.2015 21:01:31	1 day	topple	1.9 ± 0.1	2.9 - 5.9	1.1 - 7.2	5 - 8	3 - 10
	02.02.2015 17:44:10	1 day	sliding	14.7 ± 0.1	-	-	0	-
	15.02.2015 20:54:28	1 day	topple	8.0 ± 0.1	12.8 - 30.0	3.1 - 13.8	98 - 105	90 - 119
	05.03.2015 19:36:19	1 day	topple	20.7 ± 0.1	-	-	0 - 1	-
	18.04.2015 01:13:11	1 day	sliding	2.0 ± 0.1	-	-	0	-
	25.11.2015 03:54:39	27 days	sliding	94.0 ± 5	32.0 - 91.2	35.6 - 216.5	20 - 36	23 - 44
Granier	17.01.2017 21:38:12 (A_1)	6 days	-	4600 ± 50	57.9 - 192.0	108.5 - 632.5	100-160	125-189
	17.01.2017 23:20:29 (A_2)		-		15.1 - 37.4	0.8 - 2.6		127-140
	18.01.2017 01:10:18 (A_3)		-		9.0 - 21.6	2.7 - 9.3		97-107
	18.01.2017 01:12:30 (A_{4a})		-		205.1 - 948.4	570.7 - 3533.1		78-104
	18.01.2017 01:12:32 (A_{4b})		-		422.6 - 2214.5			73-89
	01.02.2017 12:14:38 (B)	13 days	sliding	11.5 ± 0.5	16.8 - 48.4	3.8 - 18.8	110-175	141-183

Table 1. Rockfall characteristics. Failure mechanism is described in section 3.1. Dating interval is based on photographic surveys and field evidences. The detachment phase is not visible for 6 Mount Saint-Eynard rockfalls (empty cells).

5 Analysis of seismic signals

5.1 Rockfall seismic signals typology

Figure 5 presents three examples of rockfall seismic signals along with their runout topography and volume. The first example (a) corresponds to a rockfall experiencing a succession of rebounds before rolling on the scree. It may have fragmented during its impacts and have mobilized loose blocks in the debris slopes while other blocks may have stopped along the slope. The second example (b) is typical of rockfalls that experience a long free-fall after their detachment. After impacting the cliff foot, the fallen compartment undergoes an important fragmentation leading to a mass flow type propagation of the blocks. The third example (c) is a more complex event. Due to the irregular topography of the cliff, the blocks experienced different propagation modes: free-fall, rebounds, and mass flow.

The analysis of seismic signals highlights the complexity and variability of rockfalls. However, it is possible to identify the propagation mode through the analysis of seismic signals. Combined movement of several particles leads to a smooth seismic signal as rebounds wave packets overlap. In the case of mass flow propagation, the simultaneous arrivals of the waves produced by a combined movement of numerous particles produce a rather smooth envelope with frequency concentrating around 5-20 Hz. In contrast, seismograms of events having suffered little or no fragmentation present irregular envelopes showing several energetic pulses. These pulses can be linked to rebounds of blocks along the cliff. As also observed by Vilajosana et al. (2008) and Bottelin et al. (2014), the most energetic phases are produced by impacts after a free-fall. These impacts generate impulsive signals with frequency contents up to 50 Hz, whereas successive block rebounds are less energetic with more emergent waveforms and frequencies up to 30 Hz.

Our goal is to link rockfall properties (failure mechanism, propagation mode, free-fall height, volume, propagation velocity, extension) with characteristics of the seismic signal (signal duration and energy, frequency content, envelope properties). The studied events display a wide variability of volume and propagation mode. Some events went through free-fall phases whereas others only rolled and tumbled down the slope. This variability of rockfall sources leads to very different rockfalls signals. Finding common relations between source properties and seismic signals is therefore very challenging. Therefore, in this study, we select only rockfalls with a free-fall phase and with a detachment seismic signal that can be isolated from the propagation phase. In order to remove the influence of the propagation mode, we focus on the first parts of the seismic signals, the detachment phase and the first impact. We assume that the rockfall compartment detached in one piece and thus that the associated seismic signal corresponds to the entire compartment detected by TLS or photogrammetry.

Figure 5. Left: seismic signal (vertical ground velocity, filtered between 2 and 50 Hz) and corresponding spectrogram. The peak amplitude of each trace, Am, is indicated in m/s. The spectrograms are computed using a simple fast Fourier transform, using a hanning taper, with a window of 128 points and an overlap between successive windows of 64 points. Right: Cliff profile for each event, the red dot indicates the starting point of the rockfall. a) 05.03.2015 Mount Saint

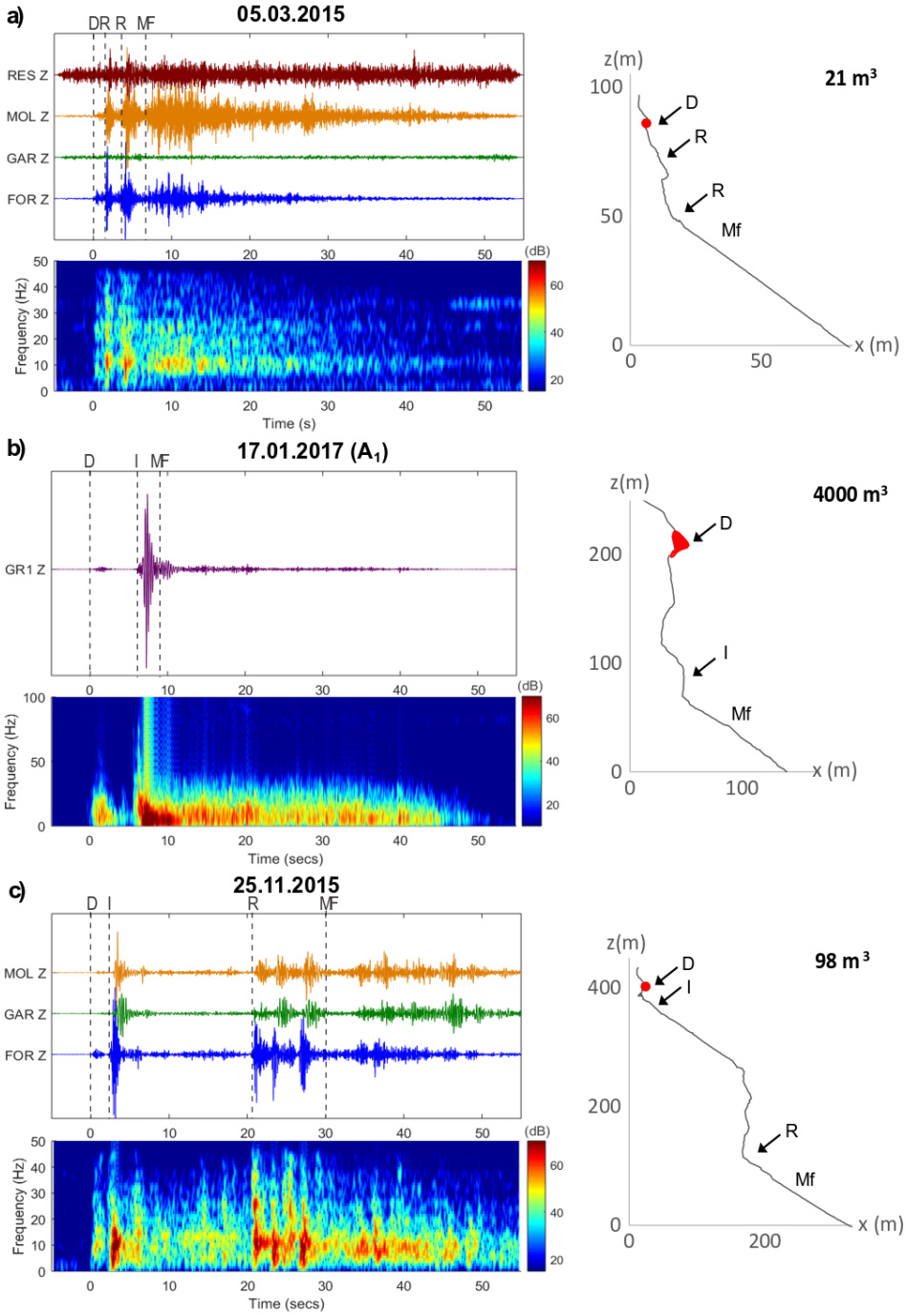

Eynard event, b) 17.01.2017 (A_1) Mount Granier event, c) Mount Saint Eynard 25.11.2015 event. Some propagation phases are identified on the seismic signal, on the spectrogram and on the cliff profile: D. rockfall detachment, R. rebound of blocks, I. impact of blocks after a free-fall, Mf. simultaneous propagation of fragmented blocks leading to mass flow.

5.2. Detachment and free-fall

The detachment phase has a smaller amplitude than the impact phase. For Mount Saint-Eynard rockfalls, the detachment phase was visible for all free-fall type events at station FOR, located on rock at the top of the cliff face. However, the detachment phase was visible only for

events larger than 6 m^3 at the other stations located on the scree slope. Although most events are not located closer to station FOR than to the other stations, the detachment phase is more visible at station FOR. This station has a better signal to noise ratio because it is located on rock and because it is farther away from the anthropogenic noise generated in the valley.

For the Mount Granier rockfalls, the detachment phase was clearly visible on all five rockfalls detected at station GRA, located 650 m away. Event A_4 was more complex, suggesting that the compartment fragmented during its detachment (A_{4a} and A_{4b}, Figure 8c). Two pulses separated by 2 seconds can be distinguished on the detachment phase. Event A_{4a}, is very small in comparison to event A_{4b} as the seismic energy of event A_{4b} is about ten times higher than A_{4a}. This separation is difficult to establish for the impact phase as the two events overlap.

The detachment phase is characterized by frequency contents around 20 Hz but in some cases up to 40 Hz (Figure 6). The duration of this phase varies between 0.5 second and 4 seconds (Figure 7a). The waveforms generally show a slowly rising and falling seismic signal.

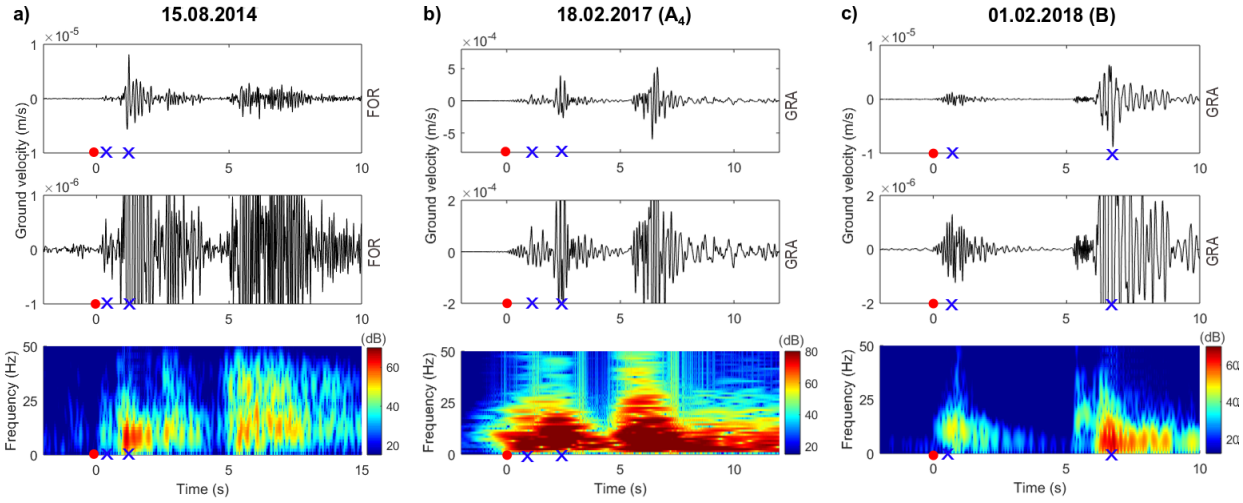

Figure 6. Detachment seismic signal, enlargement of the seismic signal and corresponding spectrogram of the a) 15/08/2014, b) 18/02/2017 (A_4) event and of the c) 01/02/2017 (B) event recorded at station GRA located at the top of Mount Granier. Red dot: initial time of the detachment phase, blue cross: maximal amplitude of the detachment and impact phases.

We investigated how properties of the detachment phase (duration and energy) scale with the rockfall volume determined by TLS V_{DEM}. We first consider Mount Saint Eynard rockfalls as a training dataset. In a second step, we test our results using Mount Granier rockfalls.

We estimated the duration of the detachment phase Dur_D recorded at station FOR. We picked manually the initial and final times of the detachment phase, because the seismic signal of the detachment phase is slowly rising and falling and because in some cases the detachment phase is not well separated from the impact phase. The duration increases slowly with rockfall volume (Figure 7a) and can be fitted by:

$$Dur_D = aV_{DEM}^b \quad (9)$$

with $a = 0.6 \pm 0.05$ and $b = 0.2 \pm 0.03$ (regression uncertainty for a confidence interval 68%) and with a correlation coefficient R^2 of 0.76.

The seismic energy of the detachment phase E_{sD} recorded at station FOR is better correlated with the rockfall volume V (R^2 =0.87, Figure 7b) and increases much faster with volume than the duration. A power-law fit

$$E_{sD} = aV_{DEM}{}^{b} \quad (10)$$

yields a = 7±3 x10^{-3} and b = 2.2±0.2.

We calculated Mount Granier rockfall volumes V_{EsD} using Equation (10). The total volume of the set of events $A_{1\text{-}4}$ is estimated to 726-3414 m^3. This represents about half of the global volume 4600±50 m^3 determined using the DEMs. The calculated volume of event B is, for its part, higher than the one obtained by the DEMs: V_{DEM}=11-12 m^3 versus V_{EsD} = 17 - 48 m^3.

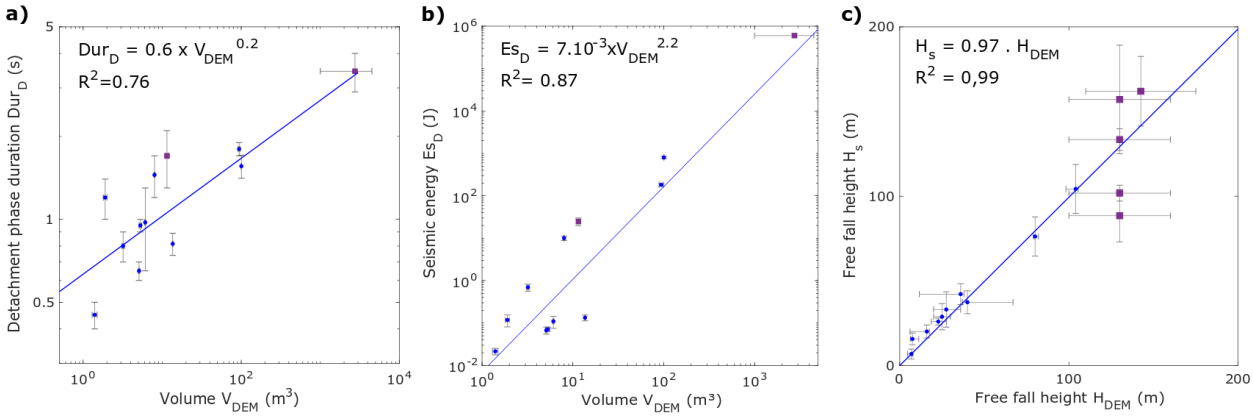

Figure 7. a) Duration of detachment phase and b) seismic energy of the detachment phase as a function of rockfall volume determined with DEMs. In a) and b), we consider only events A_{4b} and B for Mount Granier and assume a volume V_{DEM}=2850±1800 m^3 for event A_{4b} c) Free fall height calculated from the seismic signals as a function of the free fall height measured on the DEMs, Blue dots: Mount Saint-Eynard rockfalls; violet squares Mount Granier rockfalls. Straight lines are power-law fits obtained using only Mount Saint-Eynard rockfalls.

Some detachment signals are preceded by a low amplitude and low frequency (<30 Hz) phase. We interpret these signals as precursory rupture nucleation leading to the failure and detachment of the compartment. This part of the seismic signal can be isolated from the detachment signal itself by a change in amplitude and frequency content (Figure 8).

We compare the free fall height H_s estimated from the seismic signal using equation (8) with the value H_{DEM} determined on the DEMs (Figure 7c). In some cases, there is a large uncertainty on the free-fall height due to the geometry of the event (Figures 2b, 3c). For Mount Granier events, it can be observed by the marks left on the cliff, that the rockfalls have impacted two different areas: a cliff ledge or the scree slope at the base of the cliff (Figure 3c).

Uncertainties on the calculated free-fall height H_s are due to the spreading of the detachment seismic signals. However, we can see that the calculated free-fall heights are consistent with the ones measured on the DEMs with a value of R^2 of 0.98.

This result first validates our identification and interpretation of the different phases of the seismic signal: detachment phase, sometimes preceded by a precursory signal, and first impact.

Figure 8. Seismic signal for three free-fall type rockfalls a) the 18/01/2015 event recorded at station

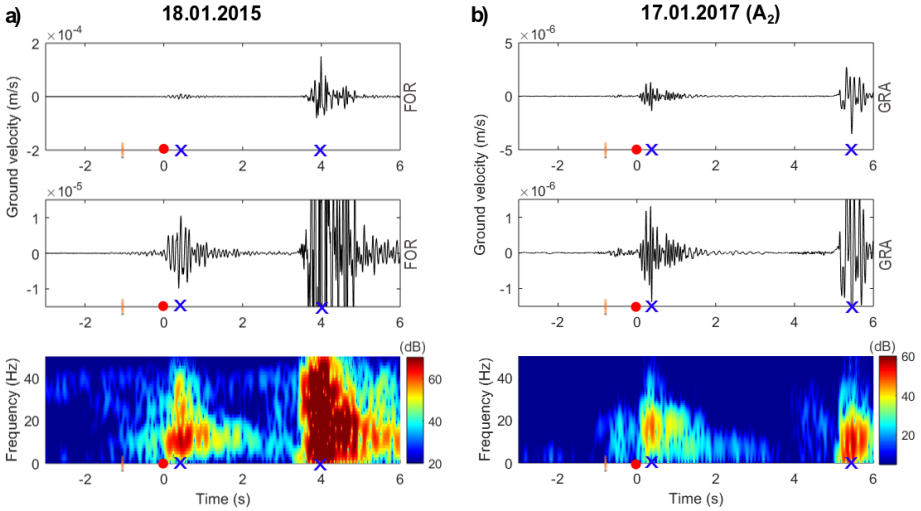

FOR station located at the top of Mount Saint-Eynard. b) 17/01/2017 (A_2) events recorded at station GRA located at the top of Mount Granier. Top: seismic signal of the detachment phase, middle: enlargement of the amplitude scale, bottom: corresponding spectrogram. Red dot: beginning of the detachment phase, orange line: beginning of a precursory phase, blue cross: maximal amplitude of the detachment and impact phases.

5.3. Impact

The seismic energy of the impact phase is strongly correlated with the potential energy. Our data for Mount Saint Eynard suggest the following relation:

$$E_{sI} = a\ E_p{}^b \qquad (11)$$

We used only Mount Saint Eynard rockfalls in order to fit a power law relation between E_{sI} and E_p (Figure 9a). The estimated parameters are a = 1±0.5x10^{-8} and b = 1.55±0.05 (confidence interval 68%) and the correlation coefficient is R^2=0.98. This fit correctly explains Mount Granier data, although these events were not used in the fit. However, this relation overestimates the seismic energy for Yosemite rockfalls. The seismic energy estimated from (11) is larger than the measured value by 7 to 50 %.

Data consistent with Hibert et al EsI = a Ep b , a=4.5x10-8±? and b = 1.38 ±?

The volume of the blocks V_{EsI} can be calculated using the following relation:

$$V_{EsI} = \frac{Ep_s}{g\ p\ H_s} = \frac{E_{sI}^b}{g\ p\ H_s} \qquad (12)$$

The computed rockfall volumes V_{EsI} are in good agreement with those determined from the DEMs (Figure 9b) with a value of R^2 of 0.99. Uncertainties on the calculated volumes V_{EsI} are related to the uncertainties on the parameters used to determine E_{sI} (V, α, r, p, c, f, see supplementary material) and H_s. This relation established for Mount Saint Eynard rockfalls has been tested with Mount Granier events. The calculated volume of event B is in agreement with the measured one (V_{EsI}: 4-19 m^3, V_{DEM}: 11-12 m^3). However, the total volume of the set of events A_1-

4 is slightly underestimated with a calculated volume of V_{ESI}=683-4178 m^3 for a measured volume of V_{DEM}=4550-4650 m^3.

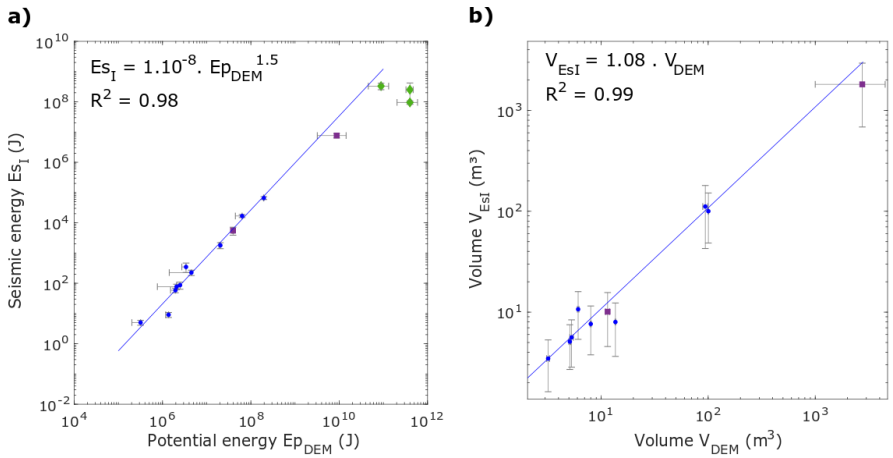

Figure 9. a) seismic energy of the impact phase as a function of potential energy calculated with DEM metrics, b) rockfall volume calculated using seismic metrics as a function of rockfall volume measured on the DEMs. Blue dots: Mount Saint-Eynard rockfalls; violet squares Mount Granier rockfalls A4 and B; green diamond Yosemite rockfall (Morrissey et al., 1999; Wieczorek et al. 2000; Stock et al., 2013). Lines are linear fits using only the Mount Saint-Eynard rockfalls.

6 Discussion

6.1 Detachment phase

In order to distinguish the detachment phase from the impact phase, the free-fall duration must be longer than the duration of the detachment phase. By combining Equations (8) and (10), we can estimate the minimal free-fall height detectable as a function of rockfall volume. For instance, for a 1 m^3 event the minimal free-fall height detectable is about 2 m whereas for 100 m^3 the minimal free-fall height is about 11 m. This drawback prevents us from studying all free-fall or topple events (3 events over 16 in the Mount Saint-Eynard data set).

We found that both the duration and the seismic energy of the detachment phase increase with rockfall volume. However, this relation is not well constrained. The scatter of these data might be due to the complexity of the detachment phase and to its variety of processes. Several factors may influence the detachment seismic signal, such as the surface of the rupture area, the detachment mode (slide, free-fall or topple), its duration, fragmentation of the compartment during the detachment, etc. However, due to the limited number of studied events and due to the lack of information on the detachment mode of these events, the influence of these factors could not be studied.

6.2 Relation between potential and seismic energy of the impact phase

The relation (11) between potential energy and seismic energy is difficult to interpret physically. The fact that the exponent *b* is larger than 1 implies that the process is not scale

invariant, the ratio of seismic to potential energy increases with rockfall size. This relation cannot be extrapolated to very large energies. Indeed, this relation predicts that the seismic energy E_p would exceed the potential energy E_p for $E_p > 3 \times 10^{12}$ J, which is of course impossible. This suggests that the relation between potential energy and seismic energy presents a change of slope for potential energies larger than 10^{10} J.

The ratio between seismic energy and potential energy $R_{s/p} = E_{sl}/E_{pDE}$ of our data ranges from 10^{-6} to 10^{-4}. This ratio $R_{s/p}$ is in good agreement with values found by previous studies. Deparis et al. (2008) estimated a ratio $R_{s/p}$ ranging from 10^{-5} to 10^{-4} for rockfalls with volumes ranging from 10^3 to 10^6 m^3, Hibert et al. (2011) found $10^{-5} < R_{s/p} < 10^{-3}$ for granular flows at the Piton de la Fournaise volcano with $1 < V < 10^3$ m^3, Lévy et al. (2015) estimated $R_{s/p} = 10^{-5}$ for volume $10^3 < V < 10^6$ m^3 and Saló et al. (2018) $10^{-6} < R_{s/p} < 10^{-4}$ for volumes $0.5 < V < 5$ m^3. Farin et al. (2015) and Bachelet et al. (2018) observed through laboratories experiments, that variations of $R_{s/p}$ could be associated with the size of the impactor and with properties of the impacted medium (e.g., roughness and bed thickness). Farin et al (2015) estimated larger values of R between 0.001 and 1 in laboratory experiments with impactors masses ranging from 0.001 to 100 g. For smooth impacted plates, this ratio increases toward 1 as the mass of the impactor increases, in agreement with their theory assuming that impact energy is dissipated as elastic energy and viscous deformation. However, for impacts on rough surfaces and for natural rockfalls, Farin et al. (2015) suggest that viscous deformation becomes negligible, and that most energy is dissipated through other processes such as plastic deformation, adhesion, or rotational modes of the impactor owing to surface roughness. Thus the value of $R_{s/p}$ can be influenced by site properties, and may be scale-dependant as we observe in our dataset.

The parameters used for the calculation of the seismic energy slightly influence this ratio. The exponent of the power law between E_p and E_S decreases with the frequency from 1.56 for a frequency of 20 Hz to 1.50 for a frequency of 5 Hz. For lower frequencies (e.g. 5 Hz), this change in exponent provides a better agreement with Mount Granier and Yosemite's events (supplementary material, Figure A.3.b). The exponent of the power law between E_p and E_s varies very little with the change of seismic wave velocity. Changing the velocity mainly affects the $R_{s/p}$ ratio.

6.3 Estimation of rockfall volume from the seismic energy of the impact phase

We have shown in this study how potential energy and free fall height can be estimated from seismic signals, allowing an estimation of rockfall volumes. However, this methodology only allows for the characterization of rockfalls experiencing a free fall immediately after their detachment. This represents 80% of the Mount Saint-Eynard rockfalls. This limitation is balanced by the improved accuracy of the results. In order to characterize all event types, it may be appropriate to calibrate a different relation between rockfall volume and seismic energy for each rockfall type.

The free-fall duration is estimated by manual picking of the detachment and of the impact phase. This is a delicate task and leads to uncertainties on both the free fall duration and on the seismic energy. In some cases, the time of maximum amplitude of the impact phase can be

significantly off the first onset of this phase. This delay might be related to several points. In a few cases, the fallen compartment may have scraped a ledge before impacting the slope (e.g. 01.02.2017 Mount Granier rockfall, Figure 6). In this case, the impact signal is preceded by a small amplitude and high-frequency wave packet. This part of the seismic signal was not taken into account in the seismic energy calculation. This delay can also be interpreted as the delay between the first contact between the slope and the compartment and the time for which the maximum energy was transferred to the slope. This explanation was assumed for most cases (e.g. 18.01.2015 Mount Saint-Eynard rockfall or 17.01.2017 Mount Granier rockfall, see Figure 8). In this case, this delay might vary depending on the volume of the compartment, on the impacted material (loose scree or cliff face) and on the slope angle. However, no clear relations appeared in our data.

The relation between seismic and potential energy has been derived for Mount Saint-Eynard dataset and then tested on the Mount Granier rockfalls. The underestimation of the Mount Granier rockfall volume (V_{ESI}=683-4178 m^3, V_{DEM}=4550-4650 m^3) may be due to the parameters used to calculate seismic energy of the impact phase. They might need to be adjusted for the Mount Granier setting to account for differences in the wave propagation medium. Another explanation can be the overestimation of the free fall height due to high uncertainties on H_s (±30 m) for events A_1 and A_4, leading to smaller volumes. The seismic energies determined for the Yosemite Park events are smaller than expected from the relation (11) obtained for the Mount Saint-Eynard rockfalls. This discrepancy may be due to the method used to estimate seismic energy from the local magnitude of the signals recorded at large distances (several tens of kilometers). This method (developed for earthquakes and assuming body waves) may produce different values from the estimation of seismic energy using Equation (2), using nearby stations (less than 2 km) and assuming surface waves. The Mount Saint-Eynard relations were determined using rockfall volumes ranging from 1 to 100 m^3. As the Mount Granier events included volumes larger than 1000 m^3, the relation (11) between E_p and E_s might need to be adjusted in order to better fit bigger volumes.

6.4 Real-time characterization of rockfalls

Real time characterization of rockfalls from seismic signals would be useful for rockfall hazard mitigation. However, developing a fully automated method is very challenging. Automatic location of rockfalls from seismic monitoring has been studied in previous works (Lacroix and Helmstetter, 2011; Hilbert et al., 2014; Manconi et al., 2016, Fuchs et al., 2018). However, in the case of Mount-Saint Eynard, the number of sensors is too small to obtain accurate locations, therefore we used rockfall locations determined from TLS or photogrammetric surveys. We have also manually checked all events detected by the seismic network to select rockfall signals, and manually picked the detachment and first impact phases. Using a fully automatic procedure may be possible using artificial intelligence methods (Hibert et al., 2014; Provost et al., 2018). Most automatic methods (artificial neural networks, random forest, hidden Markov models, support vector machines) require a training set. By coupling different methods of detection (TLS, photogrammetry, seismology), we can be confident that all events in our dataset have been correctly classified and located. Therefore, our dataset could be useful in order to develop or to test such an automatic method for rockfall detection, location and characterization. Moreover, there are

very few studies that were able to distinguish the detachment phase of rockfalls, therefore our database would provide a useful dataset in order to develop an automatic classification method.

6.5 Comparison with other studies

Previous studies, such as Deparis et al. (2008), Dammeier et al. (2011), Manconi et al., (2016) or Fuchs et al. (2018), studied scaling relations between rockfall parameters and seismic signals properties using regional seismic networks. In these studies, the distance between rockfalls and stations is much larger than in our study, of the order of tens of kilometers for regional networks compared with several hundred meters up to 2 km in our study. The rockfall volumes are also much larger (between 10^3 and 10^7 m^3) than in our study. The seismic signals are thus very different. The signals recorded by regional networks are strongly affected and transformed by the distance between event and stations. The propagation phases (i.e. detachment, impacts, mass-flow) can hardly be identified in these records. Thus, in these studies, seismic parameters (seismic energy, duration, peak ground velocity, etc.) were defined over the entire seismic signal. Deparis et al. (2008) found no clear relation between rock-fall parameters (fall height, runout distance, volume, potential energy) and rockfall seismic magnitudes. However, they found that signal duration was roughly correlated with the potential energy and the runout distance. Dammeier et al. (2011) used multivariate linear regressions combining duration, peak envelope velocity, and envelope area and found a good correlation with rockfalls volume and potential energy. Finally, Manconi et al., (2016) and Fuchs et al., (2018) proposed relationships between rockfall or rockslide volumes, and respectively duration and local magnitude. Hibert et al. (2017) carried out controlled releases of single blocks in a marl gully. They analyzed the correlation between rockfall properties and the induced seismic signals. They found that seismic energy was well correlated to the blocks kinetic energy (R^2=0.64) and poorly correlated to blocks mass (R^2=0.39).

We have compared the scaling laws between magnitude and rockfall volume obtained in these previous studies with our results. We used Equation (7) in order to estimate magnitude from the seismic energy estimated by Hibert et al (2017) and in our study. For the Mount Saint Eynard and Mount Granier database, we tested two methods for estimating seismic energy. We first selected the 18 rockfalls listed in Table 1 with a known volume V_{DEM} (excluding events $A_{1\text{-}3}$) and used the whole signal to estimate seismic energy (blue dots in Figure 10). Secondly, we selected only free-fall events and computed the seismic energy using the impact seismic signals (red dots in Figure 10). Results are shown in Figure 10 and Table 2.

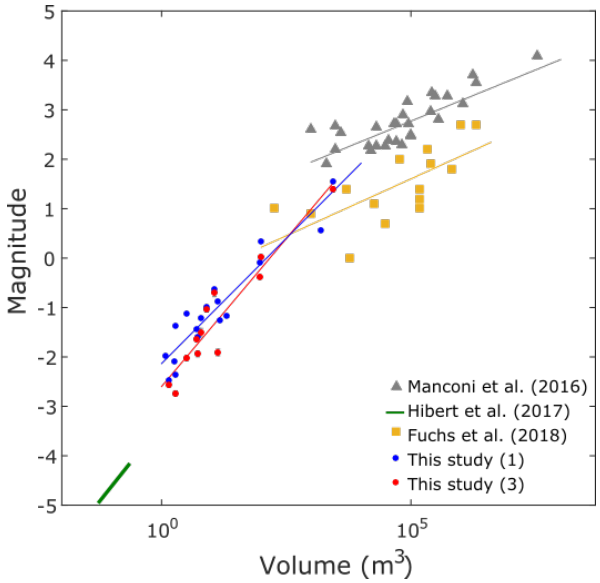

Figure 10: Magnitude of the events versus their volume. Straight lines are linear relations between magnitude and logarithm of volume.

	Scaling law	Nb events	Volume (m^3)	R^2	Median relative error on V
Fuchs et al. (2018)	M_L=-0.6+0.44log(V)	16	10^2-10^6	0.60	99%
Hibert et al. (2017)	M_L=7.4+1.3log(V)	37	0.03-0.2	0.39	-
	$M_L = X + Y \log (E_c)$	37	0.03-0.2	-	-
Manconi el al. (2016)	M_D=1.4+0.23log(V)	33	10^3-10^8	0.71	71%
This study (1)	M_L=-2.1+1.01log(V)	18	1-10^3	0.89	56%
This study (2)	M_L=-2.2+1.17log(V)	12	1-10^3	0.92	41%
This study (3)	M_L=-2.6+1.21log(V)	12	1-10^4	0.91	33%
This study (4)	M_L=-4.15+log(VH)	12	1-10^5	0.98	18%

Table 2. Scaling laws between rockfall seismic magnitude *M*, volume *V*, kinetic energy E_c (Hibert et al., 2017) and (last model) free-fall height *H*. (1) whole data set, magnitude calculated over the entire seismic signal, (2) free-fall events, magnitude calculated over the entire seismic signal, (3) free-fall events, magnitude calculated over the impact seismic signal, (4) free-fall events, correlation between potential energy and impact seismic energy.

Manconi et al. (2016) and Fuchs et al. (2018) mix different types of propagation (free-fall, sliding, rebounds), different geological settings and slope angles. This leads to a large scatter between the observed and modelled volumes. In our study, we obtain a smaller error between observed and modelled rockfall volumes, even when using all events, probably because all events come from the same site, and also because our volumes are more accurate. Selecting only free-fall

events further decreases the error. This highlights the importance of selecting rockfalls from their propagation mode. In order to remove the influence of the propagation mode of the events, we focus on the first impact. Once again, this greatly improves the accuracy of the estimated volume. Our relation (3) in Table 2 between rockfall volume and magnitude is in good agreement with the results obtained by Hibert et al. (2017) for much smaller rockfall volumes. However, Figure 10 suggests that the relation between magnitude and rockfall volume changes for volumes larger than 1000 m^3. This could explain why our relation derived for Mount Saint Eynard rockfalls with V<100 m^3 underestimates the volumes for Mount Granier and Yosemite rockfalls with V>1000 m^3.

Finally, we use the scaling relation between seismic and potential energy (11) in order to account for variations of free-fall height. This produces the strongest improvement on the estimated rockfall volume (relation (4) in Table 2). Similar results are obtained for the dataset of Hibert et al. (2017). The seismic energy is better correlated with kinetic energy than with volume. This relation yields a very accurate estimation of rockfall volume (median error of XX%), but requires an estimation of impact velocity to derive rockfall volume from kinetic energy, which is of course difficult for natural rockfalls.

The methodology presented in this paper only allows t

7 Conclusions

Monitoring rockfalls using photographic time lapse surveys and 3D reconstructions provides information such as volume, geometry, location, detachment mode, etc. The use of seismology adds information on the time of occurrence and on the propagation mode and duration of individual stages of an event. Coupling these methods at Mount Granier and Mount Saint-Eynard yields numerous information on natural rockfalls onto complex topography.

Analysis of seismic signals allows identifying several phases: detachment, free fall followed by an impact, rebounds, and granular flow. As the propagation mode strongly differs among rockfalls in our dataset, we were not able to find seismic signal features allowing a satisfying estimation of rockfall dynamics (energy, volume, etc.) for our whole data set. We therefore chose to focus on free-fall type of rockfalls and we considered only the beginning of the seismic signal: the detachment and the first impact. At Mount Saint-Eynard and Mount Granier, we have detected 15 detachment seismic signals corresponding to rockfalls of volume ranging from 1 to more than 1000 m^3.

We found a significant correlation between the seismic energy of the detachment phase and the rockfall volume. By measuring the time delay between the detachment phase and the impact phase we were able to infer the free fall heights, which are in good agreement with values estimated from the DEMs. This result supports our interpretation of the different phases of the seismic signals. We also found that the seismic energy of an impact was well correlated with the potential energy of the rockfall. Rockfall volumes can thus be calculated by using the estimated potential energy and free fall height.

The relations developed with the Mount Saint-Eynard rockfalls were then tested using the Mount Granier and Yosemite rockfalls. We found that the results were in good agreement with the measurements for the smallest Mount Granier rockfall, but slightly underestimate the largest Mount Granier rockfall (volume estimated from seismic energy is 15-89% of the volume determined using DEMs). For Yosemite rockfalls, the seismic energy recorded is significantly smaller than the seismic energy predicted by our correlation for all three events (7 to 50 %). This might be due to a

site effect or to the range of volumes of Mount Granier and Yosemite rockfalls. Our results are also in good agreement with controlled block release experiments of Hibert et al. (2017), which involved much smaller volume (0.03-0.2 m^3) than in our study.

By segregating rockfalls experiencing a free-fall from those with sliding or bouncing transport modes, and by focusing on a specific part of the rockfall seismic signal, i.e., the detachment and first impact, we were able to obtain more accurate volume prediction than other studies considering mixed propagation modes (Deparis et al., 2008; Dammeier et al., 2011, Manconi et al., 2016, Fuchs et al., 2018).

Acknowledgments

This work was carried out with the support of Géolithe, National Association of Research and Technology (ANRT), the Labex –OSUG@2020, the national project C2ROP, the program of Joint laboratories between research organizations and SMEs or intermediate-sized enterprises (LabCom) and the OMIV observatory of landslides. Mickael Langlais and Gaël Jannex are thanked for the fieldwork and data acquisition. Seismic data used in this study are available through the observatory OMIV (https://doi.org/10.15778/RESIF.MT). DEMs data are available at https://doi.org/10.5281/zenodo.2789093.
Comments and suggestions from F. Fuchs and two anonymous reviewers and from the associate editor substantially improved this manuscript.

References

Aki, K., & Richards, P. G. (1980). *Quantitative Seismology, vol. 1424*, Freeman, San Francisco, Calif.

Bachelet, V., Mangeney, A., De Rosny, J., Toussaint, R., & Farin, M. (2018). Elastic wave generated by granular impact on rough and erodible surfaces. *Journal of Applied Physics 123(4): 44901*. https://doi.org/10.1063/1.5012979.

Battaglia, J. & Aki, K. (2003). Location of seismic events and eruptive fissures on the Piton de la Fournaise volcano using seismic amplitudes. *Journal of Geophysical Research: Solid Earth, 108*. http://dx.doi.org/10.1029/2002JB002193, 2364.

Besl, P. J. and McKay, N. D.: A method for registration of 3-D shapes. *IEEE T. Pattern Anal.*, 14, pp.239-256, 1992.

Borcherdt, R. D. (1970). Effects of local geology on ground motion near San Francisco Bay. Bulletin of the Seismological Society of America, 60(1), 29-61.

Bottelin, P., Jongmans, D., Daudon, D., Mathy, A., Helmstetter, A., Bonilla-Sierra, Cadet H., Amitrano D., Richefeu V., Lorier L., Baillet L., Villard P., and F. Donzé (2014). Seismic and mechanical studies of the artificially triggered rockfall at Mount Néron (French Alps, December 2011). *Natural Hazards and Earth System Sciences*, *14*(12), 3175.

Burtin, A., Hovius, N., Milodowski, D. T., Chen, Y.-G., Wu, Y.-M., Lin, C.-W., Chen, H., Emberson, R., & Leu, P.-L. (2013). Continuous catchment-scale monitoring of geomorphic

processes with a 2-D seismological array. *Journal of Geophysical Research: Earth Surface, 118*, 1956–1974. doi:10.1002/jgrf.20137.

Burtin, A., Hovius, N., & Turowski, J. M. (2016). Seismic monitoring of torrential and fluvial processes. *Earth Surface Dynamics, 4*, 285–307. https://doi.org/10.5194/esurf-4-285-2016. https://www.earth-surf-dynam.net/4/285/2016/.

Cruden, D. M., & Varnes, D. J. (1996). *Landslides: investigation and mitigation*. Chapter 3-Landslide types and processes. Transportation research board special report, (247).

D'Amato, J., Hantz, D., Guerin, A., Jaboyedoff, M., Baillet, L., & Mariscal, A. (2016). Influence of meteorological factors on rockfall occurrence in a middle mountain limestone cliff. *Nat. Hazards Earth Syst. Sci., 16,* 719–735. https://doi.org/10.5194/nhess-16-719-2016.

Dammeier, F., Moore, J. R., Haslinger, F., & Loew, S. (2011). Characterization of alpine rockslides using statistical analysis of seismic signals. *Journal of Geophysical Research: Earth Surface, 116, F04024*. https://doi.org/10.1029/2011JF002037.

Deparis, J., Jongmans, D., Cotton, F., Baillet, L., Thouvenot, F., & Hantz, D. (2008). Analysis of rock-fall and rock-fall avalanche seismograms in the french Alps. *Bulletin of the Seismological Society of America, 98,* 1781–1796. https://doi.org/10.1785/0120070082, http://bssa.geoscienceworld.org/content/98/ 4/1781.

Dewez, T. J.B., Rohmer, J., Regard, V., & Cnudde, C. (2013). Probabilistic coastal cliff collapse hazard from repeated terrestrial laser surveys: case study from Mesnil Val (Normandy, northern France). *Journal of Coastal Research 65*. https://doi.org/10.2112/SI65-119.1.

Dietze, M., Mohadjer, S., Turowski, J. M., Ehlers, T. A., & Hovius, N. (2017a). Seismic monitoring of small alpine rockfalls – validity, precision and limitations. *Earth Surface Dynamics, 5*, 653-668. https://doi.org/10.5194/esurf-5-653-2017.

Dietze, M., Turowski, J. M., Cook, K. L., & Hovius N. (2017b). Spatiotemporal patterns, triggers and anatomies of seismically detected rockfalls. *Earth Surface Dynamics, 5,* 757-779. https://doi.org/10.5194/esurf-5-757-2017.

Eissler, H. K., & Kanamori, H. (1987). A single-force model for the 1975 kalapana, hawaii, earthquake. *Journal of Geophysical Research: Solid Earth, 92(B6),* 4827–4836.

Farin, M., Mangeney, A., Toussaint, R., Rosny, J. D., Shapiro, N., Dewez, T., Hibert, C., Mathon, C., Sedan, O., & Berger, F. (2015). Characterization of rockfalls from seismic signal: Insights from laboratory experiments. *Journal of Geophysical Research: Solid Earth, 120*, 7102–7137. doi:10.1002/2015JB012331, 2015JB012331.

Frayssines, M. & Hantz, D. (2016). Failure mechanisms and triggering factors in calcareous cliffs of the Subalpine Ranges (French Alps). *Engineering Geology, 86,* 256–270. https://doi.org/10.1016/j.enggeo.2006.05.009.

Fuchs, F.; Lenhardt, W.; Bokelmann, G. & the AlpArray Working Group, Seismic detection of rockslides at regional scale: examples from the Eastern Alps and feasibility of kurtosis-based event location, *Earth Surface Dynamics*, 2018, 6, 955-970

Guerin, A., D'Amato, J., Hantz, D., Rossetti, J. P., & Jaboyedoff, M. (2014). Investigating rockfall frequency using terrestrial laser scanner (Grenoble area, France). In *Vertical Geology Conference. Lausanne*.

Helmstetter, A. & Garambois, S. (2010). Seismic monitoring of Séchilienne rockslide (French Alps): Analysis of seismic signals and their correlation with rainfalls, *Journal of Geophysical Research: Earth Surface, 115*. https://doi.org/10.1029/2009JF001532.

Hibert, C., Mangeney, A., Grandjean, G., & Shapiro, N. M. (2011). Slope instabilities in Dolomieu crater, Réunion Island: From seismic signals to rockfall characteristics. *Journal of Geophysical Research: Earth Surface, 116, F04032*. doi:10.1029/2011JF002038.

Hibert, C., Mangeney, A., Grandjean, G., Baillard, C., Rivet, D., Shapiro, N. M., Satriano, C., Maggi, A., Boissier, P., Ferrazzini, V., & Crawford, W. (2014). Automated identification, location, and volume estimation of rockfalls at Piton de la Fournaise volcano. *Journal of Geophysical Research: Earth Surface, 119*, 1082–1105. https://doi:10.1002/2013JF002970.

Hibert, C., Malet, J.-P., Bourrier, F., Provost, F., Berger, F., Bornemann, P., Tardif, P., & Mermin, E. (2017). Single-block rockfall dynamics inferred from seismic signal analysis. *Earth Surface Dynamics, 5*, 283–292. https://doi.org/10.5194/esurf-5-283-2017, https://www.earth-surf-dynam.net/5/283/2017/.

Hoblea F., Amitrano D., Astrade L., Barnave S., Buffle A., Cardinal T., Cavalier E., Cayla N., Deline P., Gallach X, Guerin A., Hantz D., Helmstetter A., Laily B., Langlais M., Lejeune S., Le Roy G., Malet E., Ravanel L., Saint-Bézar B., Weiss J. (2018, April). Multi-method diachronic approach of the rockfalls and landslides at Mont Granier (1933 m asl, Chartreuse Massif, French Alps). In *EGU General Assembly Conference Abstracts* (Vol. 20, p. 10006).

Kanai, K., Yamabe, K., & Habasaki, A. (1984). *Study of the attenuation of seismic waves*, in Proceedings of the Eighth World Conference on Earthquake Engineering, vol. 2, pp. 273–280, Prentice-Hall, San Francisco, Calif.

Kanamori, H. and Anderson, D.: Theoretical basis of some empirical relations in seismology, *B. Seismol. Soc. Am*., 65, 1073–95, 1975

Kanamori, H., & Given, J. W. (1982). Analysis of long-period seismic waves excited by the May 18, 1980, eruption of Mount St. Helens – A terrestrial monopole. *Journal of Geophysical Research: Solid Earth, 87*, 5422–5432. doi:10.1029/JB087iB07p05422.

Kuhn, D., & Prüfer, S. (2014). Coastal Cliff Monitoring and Analysis of Mass Wasting Processes with the Application of Terrestrial Laser Scanning: A Case Study of Rügen, Germany. *Geomorphology, vol. 213,* pp. 153–65. doi:10.1016/j.geomorph.2014.01.005.

Lacroix, P., & Helmstetter, A. (2011). Location of seismic signals associated with microearthquakes and rockfalls on the Séchilienne landslide, French Alps. *Bulletin of the Seismological Society of America*, *101*(1), 341-353.

Levy, C., Mangeney, A., Bonilla, F., Hibert, C., Calder, E. S., & Smith, P. J. (2015). Friction weakening in granular flows deduced from seismic records at the Soufrière Hills Volcano, Montserrat. *Journal of Geophysical Research: Solid Earth, 120*, 7536–7557. https://doi.org/10.1002/2015JB012151.

Levy, C., Helmstetter, A., Amitrano, D., Le Roy, G., & Guyoton, F. (2018, November). *Rayleigh waves in seismic signals of rockfalls*. In 4th RSS Rock Slope Stability Symposium

Manconi, A.; Picozzi, M.; Coviello, V.; de Santis, F. & Elia, L., Real-time detection, location, and characterization of rockslides using broadband regional seismic networks, *Geophysical Research Letters*, 2016, 43, 6960-6967

Morrissey, M. M., Savage, W. Z., & Wieczorek, G. F. (1999). Air blasts generated by rockfall impacts: Analysis of the 1996 Happy Isles event in Yosemite National Park. *Journal of Geophysical Research: Solid Earth, 104(B10)*, 23189-23198.

Nicoud G., Dzikowski M., Paillet A., Ghoreychi R., Emeric P. et Chignoli M. (1999) – Données nouvelles sur la nature et l'extension du glissement historique du Granier (Savoie, France). *Actes du colloque de Myans, Documents*, 2ème série, Tome 1, 35-54.

Provost, F., Malet, J.-P., Hibert, C., Helmstetter, A., Radiguet, M., Amitrano, D., Langet, N., Larose, E., Abancó, C., Hürlimann, M., Lebourg, T., Levy, C., Le Roy, G., Ulrich, P., Vidal, M., & Vial, B. (2018). Towards a standard typology of endogenous landslide seismic sources. *Earth Surf. Dynam. (6)*, 1059-1088. https://doi.org/10.5194/esurf-6-1059-2018

Rousseau, N. (1999). *Les signaux sismiques associés aux éboulements sur l'ile de la Réunion (océan indien) - étude de deux sites : la cascade de Mahavel et la cavité de la soufrière*, (Phd dissertation). University Paris 7, France.

Saló, L., Corominas, J., Lantada, N., Matas, G., Prades, A., & Ruiz-Carulla, R. (2018). Seismic Energy Analysis as Generated by Impact and Fragmentation of Single-Block Experimental Rockfalls. *Journal of Geophysical Research: Earth Surface, 123,* 1450 78. https://doi.org/10.1029/2017jf004374.

Stock, G. M., Collins, B. D., Santaniello, D. J., Zimmer, V. L., Wieczorek, G. F., & Snyder, J. B. (2013). *Historical rock falls in Yosemite National Park, California (1857-2011)* (p. 17). US Department of the Interior, US Geological Survey. https://pubs.usgs.gov/ds/746/Yosemite_rock_fall_database_narratives_1857-2011.pdf

Teza, G., Pesci, A., Genevois, R., and Galgaro, A.: Characterization of landslide ground surface kinematics from terrestrial laser scanning and strain field computation, *Geomorphology*, 97, pp.424-437, 2008.

Varnes, D.J. (1978) Slope Movement Types and Processes. In: Schuster, R.L. and Krizek, R.J., Eds., Landslides: Analysis and Control, National Research Council, Washington DC, *Transportation Research Board, Special Report* 176, National Academy Press, Washington DC, 11-33.

Vilajosana, I., Suriñach, E., Abellán, A., Khazaradze, G., Garcia, D., & Llosa, J. (2008). Rockfall induced seismic signals: case study in Montserrat, Catalonia. *Nat. Hazards Earth Syst. Sci., 8,* 805-812. https://doi.org/10.5194/nhess-8-805-2008.

Wieczorek, G., J. Snyder, J. Waitt, M. Morrissey, M. Uhrhammer, R. Harp, E. Norris, R. Bursik, and M. Finewood (2000). The unusual air blast and dense sandy cloud triggered by the July 10, 1996 rock fall at Happy Isles, Yosemite National Park, California, *Geol. Soc. Am. Bull. 112*, 75–85.

Zeckra, M., Hovius, N., Burtin, A., & Hammer, C. (2015). *Automated detection and classification of rockfall induced seismic signals with Hidden-Markov-Models*, 2015 AGU Fall Meeting 2015 – NH34A-04.

Zimmer, V. L., Collins, B. D., Stock, G. M., & Sitar, N. (2012). Rock fall dynamics and deposition: an integrated analysis of the 2009 Ahwiyah Point rock fall, Yosemite National Park, USA. *Earth Surface Processes and Landforms*, 37(6), 680-691.